

Canadian Hyperloop Conference Design Documentation
April 2022

Table of Contents

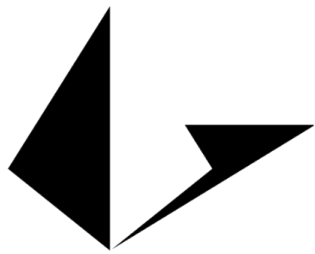
Team Description	4
Brake Dynamometer	6
Overview	6
Dynamometer Controls	9
Testing.....	11
Full Pod Preliminary Design	12
Structural	12
Guidance	17
Vertical Stability	17
Horizontal Stability.....	20
Powertrain	22
Pressurized Systems.....	24
Braking	26
Battery System	29
Electricals	30
Software comms and controls	34
Appendix	37
Frame FEA responses.....	37
Stability Mechanical Analysis	40

Sponsors

Thank you to our sponsors, Würth Electronics, Loopring, and Altium for their support in our endeavor to develop Hyperloop technology.



**WÜRTH
ELEKTRONIK**
MORE THAN
YOU EXPECT



LOOPRING

Altium®

Team Description

The Cooper Hyperloop Team is a student-run extracurricular organization at The Cooper Union for the Advancement of Science and Art. It is based in New York City and focuses on designing and building a Hyperloop pod in an effort to further the development of Hyperloop technology. Cooper Hyperloop was founded in 2019 with the intention to compete in the SpaceX pod competition. In its first year it placed in the top 40 teams. Since then, the team participated in The Hard Tech Fund's symposium in the summer of 2020 and participated in European Hyperloop Week in the summer of 2021. The team has been improving the pod design since then enlarging from three subsystems to five; adding power and frame subsystems. The team consists of about 25 students from Mechanical Engineering, Electrical Engineering, and Civil Engineering majors, across all four years.

About Cooper Union

The Cooper Union is a small, elite 900-student college located in the heart of New York City. It has three main schools: Architecture, Art, and Engineering. The student body is a close-knit community and has an intense work ethic. The school was founded upon the belief that education should be free and accessible to all, regardless of race, religion, or class. At The Cooper Union, students get individual attention and have the ability to participate in extracurricular design teams such as Hyperloop. Since Cooper Union is such a small school, the team has limited resources and a limited budget, and this encourages Cooper Hyperloop to be as strategic and economical in designs as possible.

Vision Statement

Cooper Hyperloop aims to advance the feasibility of vacuum transport technology. By contributing Cooper Union's brightest minds towards building Hyperloop vehicles, we hope to make high-speed, clean transportation a reality.

Team Members

Aaryan Mahipal:	Power	Hadassah Yanofsky:	Business Lead
Aditi Pattabhiraman:	Thermals Lead	Irene Choi:	Business
Afifa Areya:	Brakes	Petros Sklavounos:	Frames Lead
Alexander Landinez:	Brakes	Richard Lam:	Technical Team Lead, Stability Lead
Ari Gebhardt:	Comms & Controls	Saira Billah:	Stability
Azra Rangwala:	Power	Sam Shersher:	Team President, Power Lead
Darius Fantozzi:	Brakes	Shahrin Khan:	Stability
Effie Bluestone:	Comms & Controls	Vlad Bershchanskiy:	Business
Eli Sadek:	Frames	Yaacov Davidowitz:	Brakes Lead
Franklin Cevallos:	Comms & Controls	Yu Shan Luo:	Comms & Controls
Gary Kim:	Comms & Controls Lead	Professor Phillip Yecko:	Faculty Advisor



Brake Dynamometer

Overview

The automated test rig (“brake dynamometer”) is designed to run tests to determine optimal metrics for a braking system prototype. It is useful to confirm the veracity of the simulations done of the braking system, particularly because of the use of Eddy Current braking, which tends to be hard to simulate. The dynamometer is also able to test the integration of basic brakes, communications and controls, and power systems; before finishing the designs of all the systems and integrating them into the pod. The brake dynamometer was designed with safety having the highest priority. The brake dynamometer consists of four subsystems:

1. A communications and controls subsystem that is responsible for the automation of the brake dynamometer
2. A powertrain which accelerates a flywheel up to 4850 RPM
3. A pneumatic system which actuates the brakes
4. An eddy current brakes system

Each of these subsystems are designed such that the brakes engage during any emergency condition, including power loss.

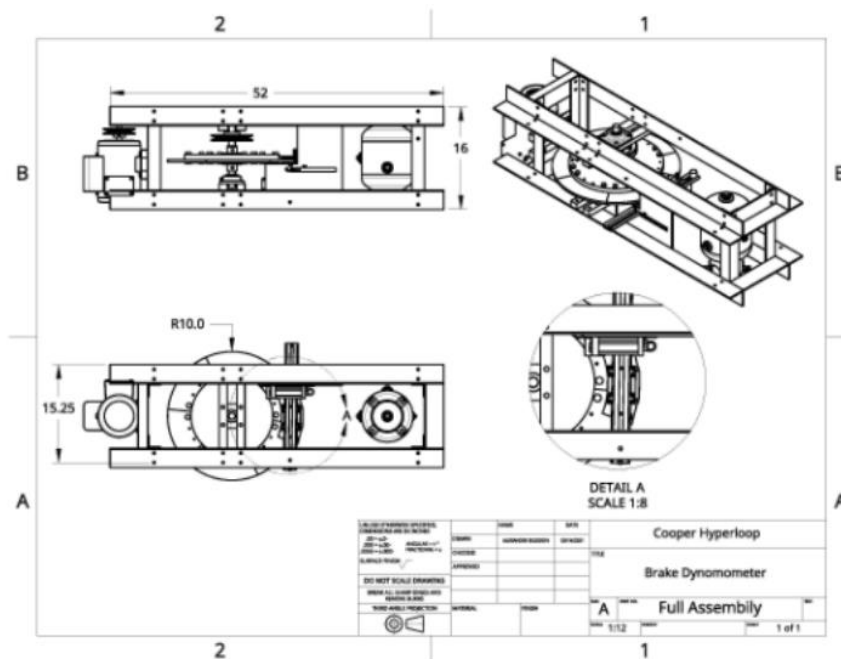


Figure 1.1 Drawing of the brake dynamometer (units in inches)

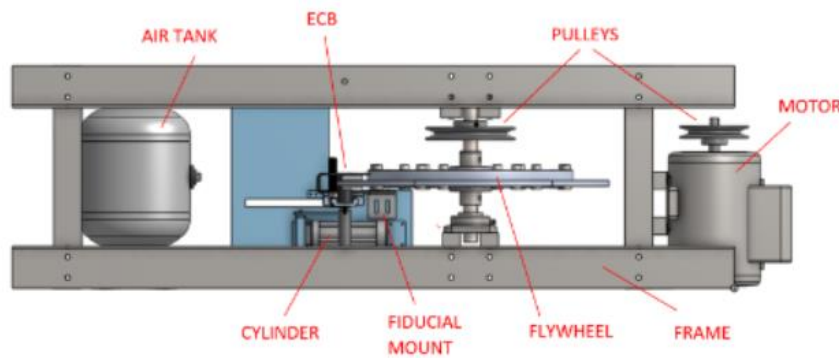


Figure 2.2 Labeled view of important mechanical parts

General Assembly and Functionality Overview

The main function of the brake dynamometer is to test how the Eddy Current brakes will brake on the full track. The dyno operates with a motor spinning a flywheel up to approximately 2500 RPM, which represents the track. When the brakes are engaged remotely, the motor stops, and the pneumatic cylinder retracts, which engages the brakes. As the brakes engage, a flange attached to the brake mount hits a force sensor, which measures the braking force.

Powertrain System

The powertrain in the brake dynamometer system uses a motor to accelerate the flywheel. The motor used in this system is a ½ HP general-purpose motor with a max 3450 RPM and a breakdown torque of approximately 4 N-m. The motor delivers power to a flywheel through a pulley-and-belt system, which uses an adjustable length quick link v-belt. This pulley-and-belt is on a 5.2 : 3.7 ratio, therefore the maximum RPM of the flywheel is geared down to 2500 RPM. The flywheel used in this model is constructed out of 6061 Aluminum in several pieces, a central disk and six edge pieces weighing 0.51kg(1.125lbs) each. The flywheel has been balanced to omit vertical oscillation in its motion.

Pneumatics Actuation

The dynamometer uses pneumatic actuation to engage the ECB array along the flywheel. A 50 psi air tank (12-lbs Compressed Air Tank; 200 psi) was deemed necessary based on the amount of times the brakes will need to be engaged throughout one run. The compressed air tank will be connected to a 20 psi regulator to bring the air pressure down to what is required for the linear actuator. A digital pressure switch senses the pressure at the output of the regulator, ensuring it falls within the operating range. This data is sent to the ESP 8266 microcontroller and to the braking board directly. The air then flows through an active low 5/2 valve. Two chokes limit the flow rate at the input and output of the cylinder, so that actuation and de-actuation speeds can be controlled separately.

Finally, the air flows to the cylinder, which actuates the brakes. A tie rod cylinder, with two parallel piston rods, was used. The cylinder is coupled to a linear guide rail with a linkage that converts the linear movement of the actuator to a rotational motion that sweeps the guide rail and Eddy Current Brake (ECB) into braking position. Once the brakes are engaged, the reaction force will cause them to quickly slide into a load cell, which will measure the reaction force of the flywheel on the ECB overtime and

record the force data. This setup will be used in prior testing to characterize the ECB by gathering speed-force curves.

Dynamometer Controls

High Level Overview

An ESP8266 microcontroller is used to control the various parts of the brake dynamometer automated test rig. A single ESP8266 is used as it has enough GPIO pins to control all parts of the test rig and collect data from all sensors. This microcontroller controls power to the motor with a relay, controls brake actuation, and monitors various sensors to determine the speed, forces, and status of the test rig.

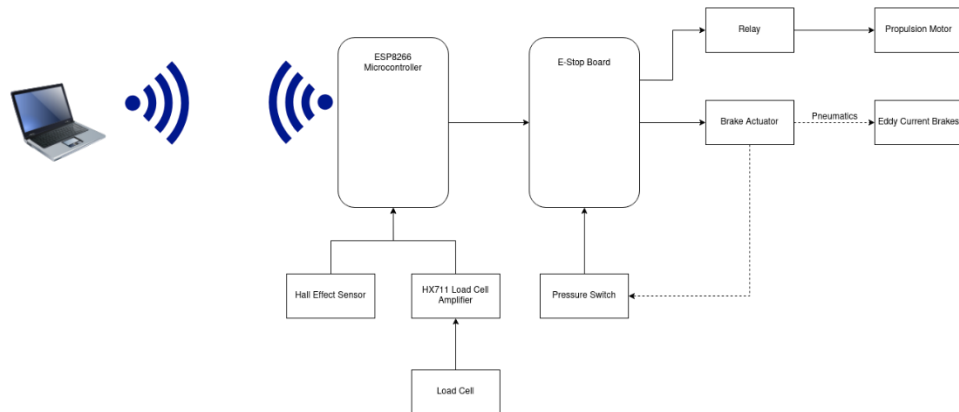


Figure 3.3 Automated Test Rig Control System

Communication with Controlling Computer (Brake Dyno)

Communication between the microcontroller and controlling computer is done using 2.4 GHz 802.11n wifi. The ESPHome API (Application Programming Interface), which works by sending Google Protobuf messages through a TCP connection between the computer and microcontroller, is used to control and collect data from the ESP8266. All data collected is made available to view by the controlling computer live or by saving into a CSV file on the system for future analysis.

Various APIs were also considered for communication between the microcontroller and controlling computer but were all determined to be either unnecessary or excessively complex. Another option that would have been easy to implement would have been communication via MQTT. MQTT is a lightweight network protocol that allows devices to subscribe to and publish data to channels. If data is published to a channel, any other device subscribed to that channel will receive the information. While this would have worked fine, it added another required service to run in the form of the message broker and none of the advantages provided by MQTT was an advantage not also provided by the native ESPHome API. A simple REST over HTTP API was also considered. While a REST API was exceptionally simple to implement and therefore was also the first API used for testing, it very quickly became clear that it was too slow and computationally heavy for the ESP8266 microcontroller to handle. Out of the options available, the native ESPHome API had an acceptable overhead and was easy to implement.

Load Cell

The test rig has a wheatstone bridge loadcell installed to measure the lateral force placed on the eddy current brakes. This load cell is connected into a HX711 load cell amplifier to report the load on the load

cell digitally to the ESP8266 microcontroller. The ESP8266 then loads the data from the HX711 load cell amplifier and reports it to the controlling computer.

Operation Sequence (Brake Dyno)

When the program begins, the device is in brake mode, where the motor is off and the brake are engaged. By sending a start command, the brake dyno enters standby mode where the brakes are disengaged. Once in standby mode, a drive command is required to enter the acceleration state, where the motor is turned on. Once the flywheel reaches a target speed, as detected by the hall effect sensor, the flywheel enters coast mode, where the motors and brakes are off and the flywheel remains spinning. After a set time, the brake dyno returns to brake mode and the brakes are reengaged.

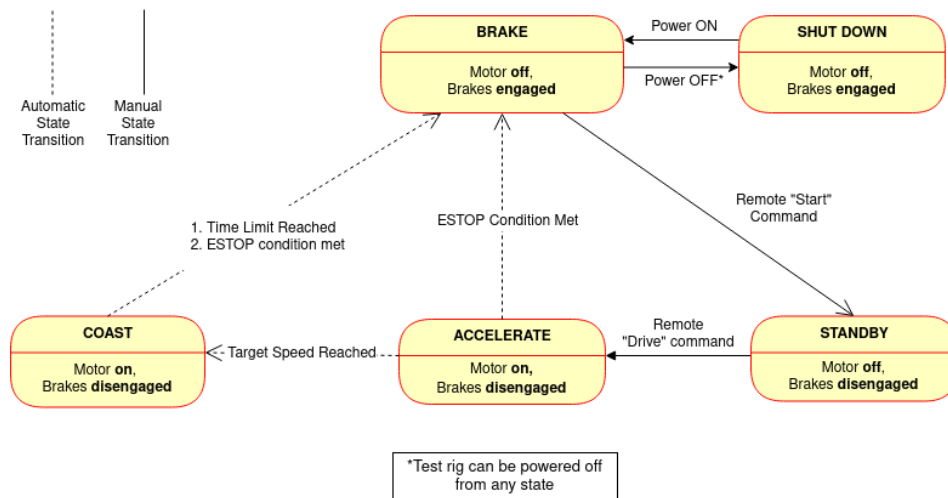


Figure 4.4 Automated Test Rig State Diagram

A separate debug mode is also available that grants the operator access to the raw data of all sensors and direct control of everything that the microcontroller can access. Access to this mode can be password protected.

A password protected remote over the air update mode is also available for quickly updating the firmware on the microcontroller during a test if necessary.

Contingencies

The ESP8266 microcontroller is programmed to expect a safety ping from the controlling computer at least once per second. If this interval is missed, the pod or test rig will assume that the controller has either crashed, disconnected, or is otherwise unavailable and will disable the motor then engage the brake to bring the pod or test rig into a safe mode. To come out of test mode, the microcontroller must be power cycled.

The ESTOP board was created as another safety failsafe. It implements the most basic parts of our failsafe system as hardware logic to isolate it from any potential software bugs or failures. The ESTOP board requires an all-clear signal from all electronic components on the pod to stay enabled. If any all-clear signal is interrupted, a T flip-flop is switched and the ESTOP board goes into failsafe mode. In this mode, the motor is instantly turned off then the brakes are engaged to bring the pod to a safe stop. This ensures that, for example, if pressure in the pneumatic system shows signs of leakage, the all-clear signal for the pneumatic system drops and the ESTOP board will disable the motor and engage the brakes with the leftover pressure. To come out of failsafe mode, all all-clear signals must be restored and a separate, otherwise unused, reset signal must be sent to the ESTOP board which will cause it to check that all all-clear signals are re-enabled then, if they are, return control of the test rig to the microcontroller.

Testing

The eddy current brake design was tested with an automated test rig to determine the braking force applied. The objective of this test run is to demonstrate the magnetic force generated from varying number of arrays and the spacing between them. By taking those parameters as inputs, the system integrated within the brake dynamometer will yield maximum output force at given speeds of the flywheel. The graphs generated in Figure 5 demonstrate two separate test runs documenting the braking force resulting from the ECB and speed of the flywheel. From the relationship observed, there is a brake force generated at high speeds. The flywheel in the test rig can spin up to approximately 2500 RPM. Once the ECB array is actuated to decelerate the flywheel, it can apply a maximum force of 160 Newtons. These results are primarily based on the current design of the array in the automated test rig, which has 12 pairs of magnets placed along a curved C-channel (24 total magnets). However, based on the derived relationship as shown in Figure 5, with increased set of magnets along the array, a greater force can be generated at higher speeds. Therefore, a linear array can be constructed for the pod.

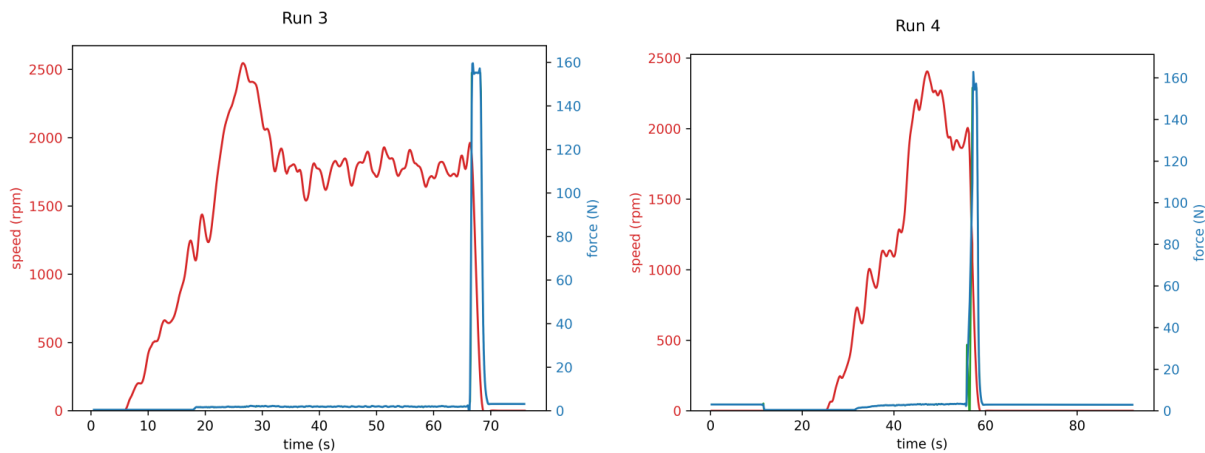


Figure 5. Sample of test results from the Brake Dynamometer demonstrating the relationship between braking force and speed over time.

Full Pod Preliminary Design

Structural

A comparison study conducted for the choice of hollow square beams or c brackets

The cross-section that is optimal for the frame was determined with the projected forces and directions being 1800N axially through each hole. To test the cross sections and compare them, primary FEA analysis was done on a hollow square beam and a c-bracket with axial and downward forces of equal magnitude with comparable lengths, which is shown in the Appendix. These tests comprised of an equal magnitude of force being applied on the comparable face to observe the cross-section's response. The material chosen was consistently chosen to be an arbitrary aluminum 1060. The fixture was at the bottom of each geometric shape. Below is table highlighting Solidwork's results when running these simulations to compare them. A hollow square beam was found to be most structurally rigid.

Using nodal 'highlighting' on areas of interest (shown in Appendix), an insight into zero stress areas is gained and will aid in future topology optimization of the frame.

Data table for comparison

Measures	Hollow Square beam	C bracket beam
Top load deformation scale	3275.9	206.3
Top load Factor of safety minimum	8.9	2.1
Axial load deformation scale	1112.38	383.167
Axial load Factor of safety minimum	5.2	2.6
Greater than yield stress top load?	No	No
Greater than yield stress axial load?	No	No
Ratio of yield stress top load, highest to yield	0.116	0.519
Ratio of yield stress axial load, highest to yield	0.193	0.388

Frame design iterations:

1) Entirely square beam frame

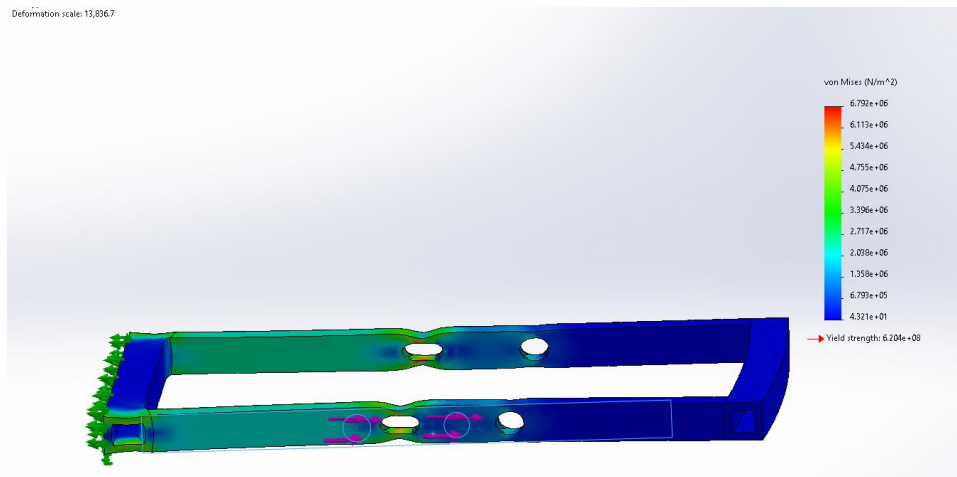


Figure 6. As seen, this assembly did not withstand applied forces, displacement of holes is great and the stresses are greater than yield.

2) Using I-beams to carry axial load

Using I-beams to carry the axial load is a more robust design as the line of action acts through the line of symmetry of the I beam, where there is mass to act through, while the hollow square beam had a smaller thickness. Using a small section of I-beam, primary FEA analysis is conducted to see if there is failure with this geometry for the desired applied loads. The material used is Aluminium 1060.

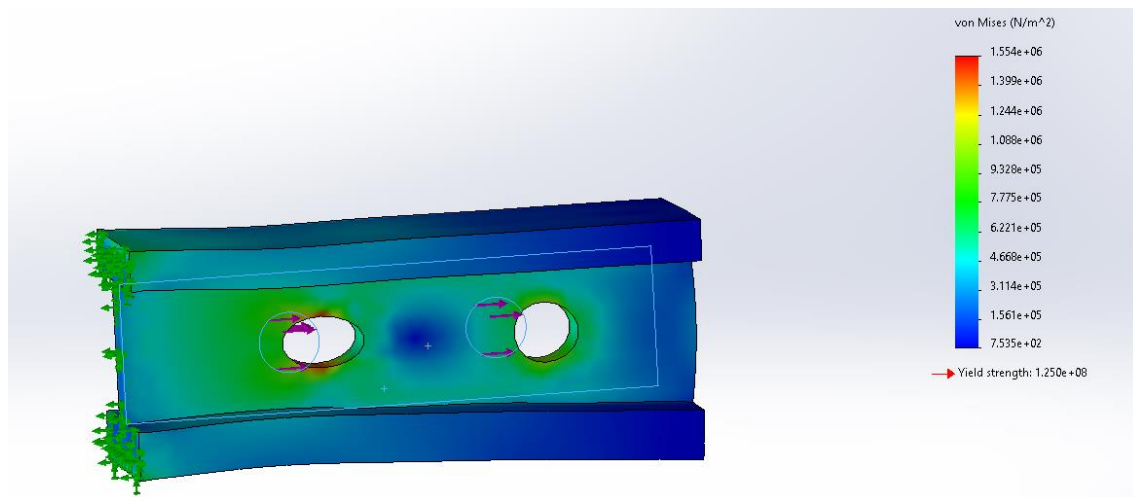


Figure 77. The maximum stress is a couple of orders away from the yield strength of the material.

3) Using tubes instead of hollow square beams as connectors

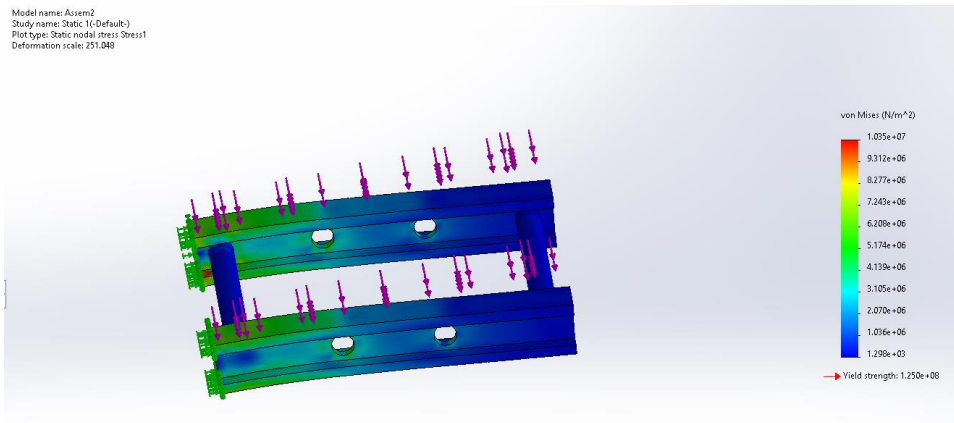


Figure 88. Not optimal deformation displayed, with high areas of stress

Comparison between tube and hollow square beam cross section for connectors

Equal area, material and force is used to make these different geometries comparable. The end goal is to minimize weight hence using hollow beams and aluminum alloys.

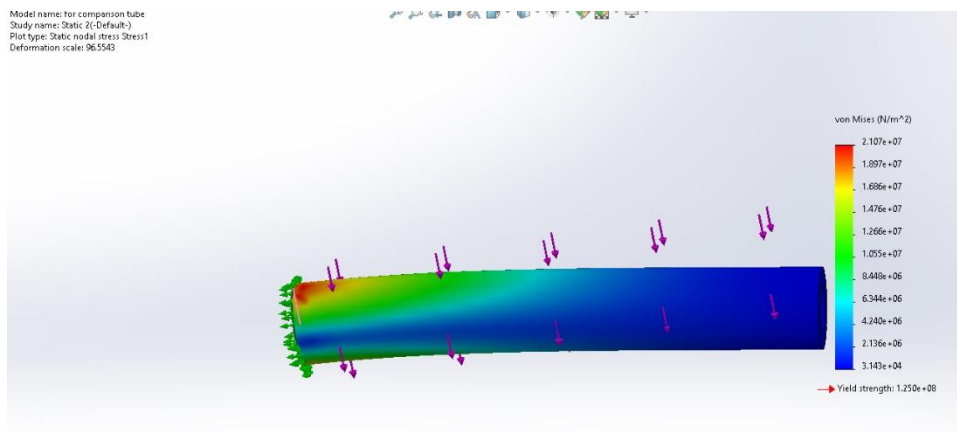


Figure 9 9. Von Mises' stress analysis. A constant force and cross-sectional area is tested and compared to the below figure. At the base of the fixture there is a high stress concentration

Deformation scale: 992.475

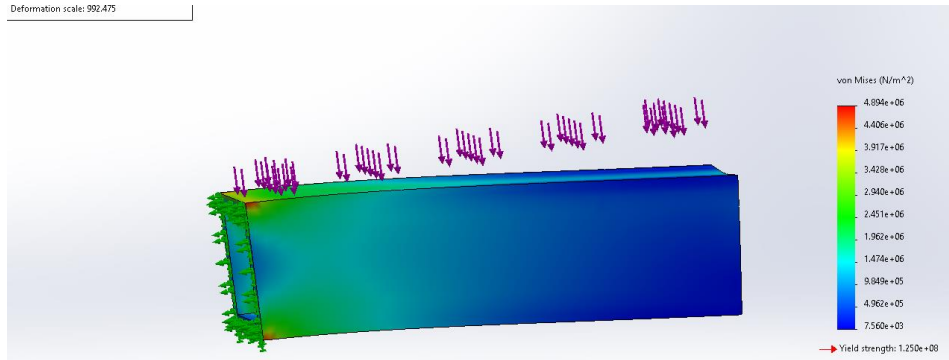


Figure 10. Von Mises' stress analysis. A constant force and cross sectional area is tested and compared to . At the base of the fixture there is a lower stress concentration, as well as across the body in comparison to the cylinder cross section.

A downward force was used to test their strength in an arbitrary distance and compare them. Majority of the direction of the force felt by these connectors would be in the downward force due to the weight of the components that are mounted onto the frame. While strain is important, square brackets lower the maximum stress.

4) First iteration of frame assembled using above analysis

A frame made up of I-beams and hollow square beams as connectors was assembled and testing under the design constraints. The results show a significant number of orders away from the yield stress of the material, with no failure and little-to-no areas of high stress concentration.

The constraints of the frame are that the 'sides' need to be able to withstand the braking force of the braking system through the mounting holes. The top part has to be flat in order to mount other components with L-brackets and bolts. The frame is to be lighter than last year's attempts (it was about 80lbs), while staying within the budget.

Deformation scale: 18,385.6

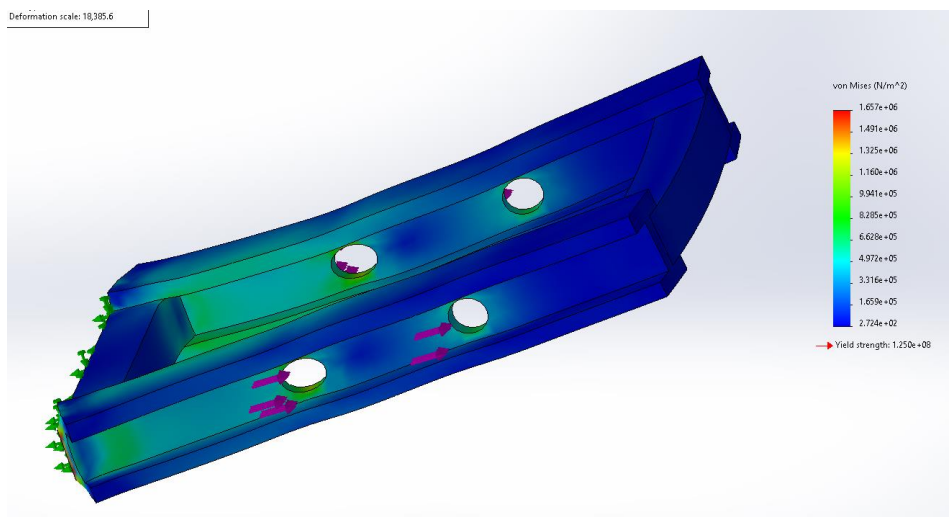


Figure 11 11. Overhead view of the third iteration of the frame, where no plastic deformation occurs.

In order to manufacture this structure, there have been design revisions and a material analysis decision matrix conducted. Below is the material analysis decision matrix.

Steel							
Material	Yield Stress(ksi)	Shear Modulus (ksi)	Modulus of Elasticity (ksi)	Density (lb/in ³)	Applicable Shape	Cost	Section used for cost
A36	36	11300	29000	0.28	Channel	\$23.40	C channel 3/4 X 3/8 X 1/8 web - 4 ft
A572 Gr. 50	55	11600	29000	0.28	I-beam	\$90.50	S 3 x 5.7# (3.00" x .170" x 2.33") - 5 ft
A513 Gr. 1010	42	11900	29000	0.28	Tube	\$14.16	1 OD x .083 wall - 4 ft
A500	46	11600	29000	0.28	Tube	\$14.56	1.05 OD X .113 wall - 4 ft
Aluminum							
Material	Yield Stress(ksi)	Shear Modulus (ksi)	Modulus of Elasticity (ksi)	Density (lb/in ³)	Applicable Shape	Cost	Section used for cost
6061-T6	40	3770	10000	0.098	Channel	\$33.00	2 x 1 x .130 web - 4 ft
6061-T6	40	3770	10000	0.098	Tube	\$21.82	1 OD x .125 wall - 4 ft
6063-T52	21	3740	10000	0.1	Tube	\$16.79	1 OD x .125 wall - 4 ft

Table 1: Material Analysis decision matrix

The above properties were researched for different alloys of steel and aluminum. Material cost, weight, and yield stress were the most important factors considered. The aluminum alloys have a yield stress comparable to steel while having a much lower weight. However, this comes at a higher cost. A513 steel has a desirable yield stress and is the cheapest of the materials researched. A513 steel and 6063 aluminum appears to be the best options, and which one is ultimately utilized depends on whether yield stress or weight is prioritized. These are all frame decisions and research that has been done for the frame to come, for the time being, the frame has been kept to L-brackets connected by an I-beam.

Guidance

Vertical Stability

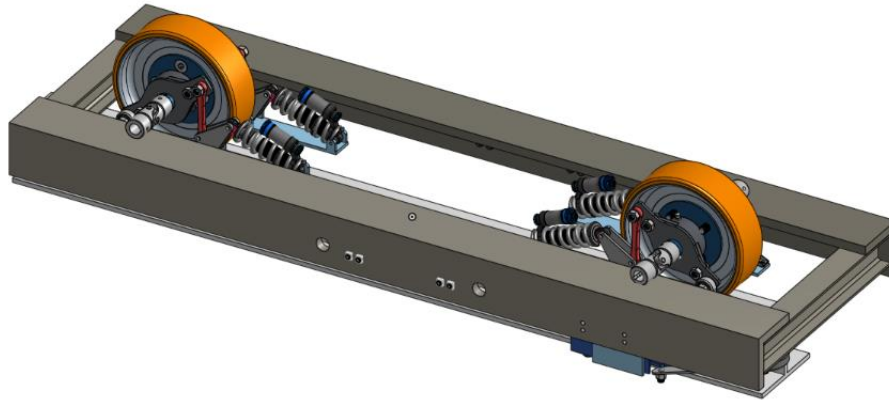


Figure 1212. Vertical Stability mounted onto frame

The main objective of the vertical suspension system is to improve the dynamics of the pod during acceleration and cruising to ensure that vibrations from the track do not cause loss of control of the pod or damage any onboard components. To accomplish this, the suspension isolates the wheel mass from the pod and provides damping to the system and controls the ride height such that the eddy current brakes will always overlap the flanges of the I beam, and the horizontal suspensions stay within the clearances of the track. The cantilever type suspension translates the vertical motion of the wheel into travel in the suspension, while the universal joints attached on either side of the wheel transmit the torque from two motors to the wheel while still allowing vertical displacement. While the exact specifications of the pod have yet to be determined as the full pod is yet to be finished, the dimensions of each part and the suspensions were chosen based on our target velocity and target pod mass.

Suspension Geometry:

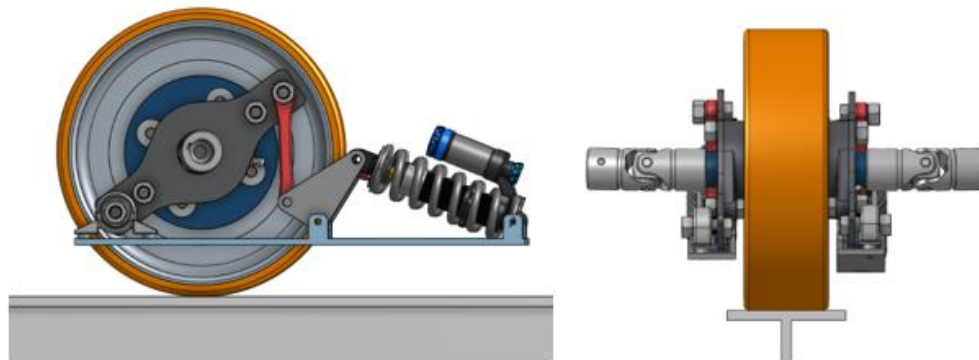


Figure 1313. Side view (left) and front view (right) of the vertical suspension

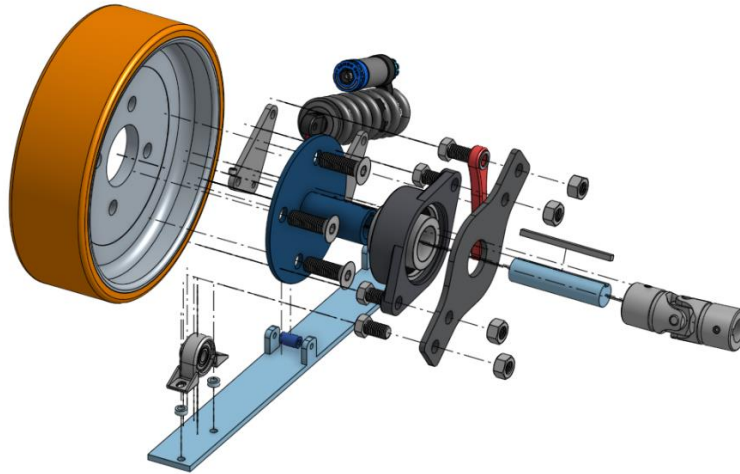


Figure 1414. Exploded view of Vertical stability

To allow the wheel to be driven by the motor, the wheel hub is attached to a universal joint by a keyed axle. The wheel hub axle is then mounted to the suspension arms by a mounted high-speed bearing which connects the rotating elements to the static members. The suspension arms consist of a main lever arm where the wheel bearing is mounted, a tension rod (red), a rocker and the suspension spring. The main lever arm rotates about a bearing (bottom left), creating a third-class lever that pulls the tension rod. The tension rod then pulls the asymmetrical rocker (3" by 1.5" side lengths) to compress the suspension spring. The advantage of this design is the mechanical advantage created by the main arm and the asymmetry in the rocker, amplifying the vertical displacement of the wheel to create more travel in the suspension. The geometry creates a 3.78:1 mechanical advantage between the suspension travel and the wheel displacement, which allows a cheaper and smaller suspension to be used, as the wheel rate is much greater than the spring rate. A graph of the vertical displacement of the wheel against the suspension travel is shown in figure 15. The wheel rate can be adjusted by changing the side lengths of the rocker, which is a significantly cheaper option than replacing the entire shock. Furthermore, the design allows for ride height adjustability, as the length of the tension rod can be shortened or lengthened to increase or decrease distance between the frame and the track.

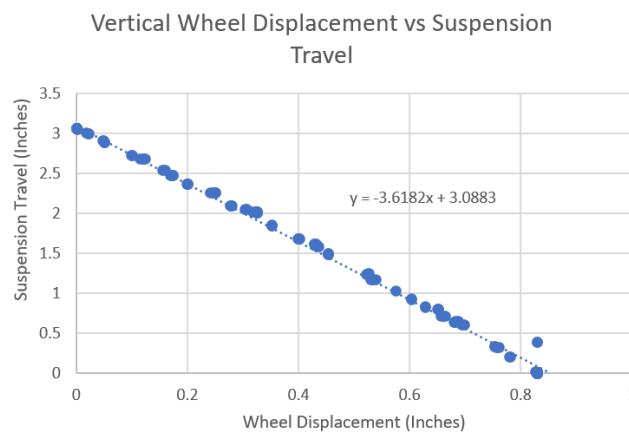


Figure 1515. Graph of vertical displacement vs suspension travel

Another advantage of the design is that the only parts manufactured in house are the base plate and the main lever arm. All other parts are common to other vehicles and therefore do not need to be manufactured in house; the wheel and hub are commonly found in go-karts and the tension rod and rocker are found in motorcycle linkage suspensions. This reduces manufacturing cost and increases iteration speed, allowing us to rapidly test our design.

Wheel Considerations:

In order to withstand the high velocity of the pod and the large load, an optimal wheel was sourced for the stability system. Many factors were considered when choosing this wheel such as hardness, shape, type of wheel, mounting configuration, and size constrictions. Given that the wheel would be running on an aluminum 6061 track, it would need enough friction to avoid slipping. The necessary friction coefficient was determined 0.204 as observed in Equation 1.

Comparing this coefficient against existing friction coefficients of plastics and metals, a polyurethane material was the best fit for the wheel. This material can be found in the form of a foam, a coating, or just a solid wheel. Rubber tire pneumatic wheels were also thoroughly researched as a type of wheel to consider, however given our size constraints and our non-hub motor set up, pneumatic wheels were too large to source and did not add any advantage to our design.

With further research, roller wheels were determined to have the best application for our case. They translate motion well and run smoothly on smooth surfaces with enough traction. Given these findings, a proper wheel for our set up would need to have a metal core with a polyurethane coating. In order to mount the suspension system onto the wheel, it was also ideal for the wheel to have a universal mounting hub which is easier to source and would allow for simpler geometry. Since the suspension system would be mounted on both sides of the wheel, it was also necessary that the driven wheel have a symmetric hub system.

Once figuring out the proper material and type of wheel, we were able to determine the dimensions of the wheel. In order to maximize the traction of the wheel, the width would need be maximized as well. Since the I-beam is 5 inches wide, the ideal range for the wheel width was between 3-4 inches in order to allow space for the suspension system. As for the wheel diameter, it was observed that larger wheels could withstand higher loads and higher velocities, so we aimed for a wheel that was between 10-16 inches in diameter. The upper range for radius of the wheel calculation can be observed in Equation 2. These requirements were met by Model 235GBA3025 which can be classified as a mid-roller wheel with a diameter of 11.8 inches that can withstand up to 750 kilograms of loading. The decision matrix used to narrow down the wheel options can be found below.

Model:	Price(\$):	Diameter(inches):	Width(inches):
4991T28	66	13.3125	4.5
22865T37	244.93	14	3
W-1030-SWF-3/4	494.26	10	3
235GBA3025	645	11.8	3.54

Table 2: A decision matrix to narrow down wheel options

Horizontal Stability

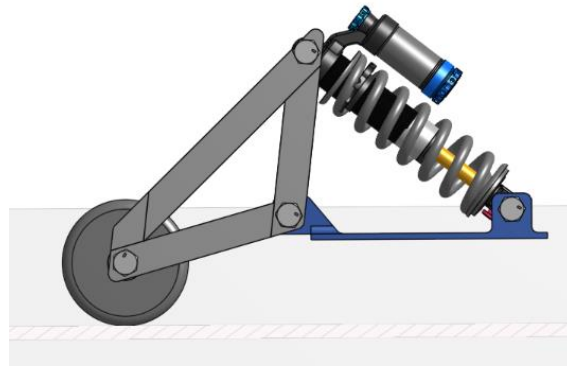


Figure 1616. Side view of the horizontal stability geometry

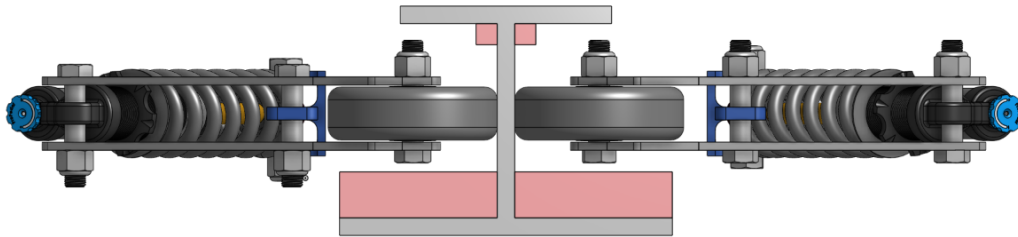


Figure 1717. Horizontal stability on the I-beam. Clearances are in red.

The horizontal stability limits the lateral motion of the pod and controls yaw and roll of the pod. The design chosen was intended to be easily manufacturable and modular, allowing for easy adjustment once a full pod is designed. The horizontal suspension wheels interact with the web of the I beam, staying within the clearances of the I-beam specified by the CHC rulebook (shown in red). The suspension is a cantilever design that translates the lateral motion into compression in the spring through the rocker arms. The rocker and base are both constructed using welded 1" x 3/16" steel plates, lowering the cost and difficulty to manufacture.

The horizontal stability was modeled by assuming the wheel is rigid, and thus follows the I beam exactly. A half model and full model of the vehicle was designed using the following free body diagrams (Figure 16, Figure 17), and were evaluated based on the angular and lateral displacement of the vehicle.

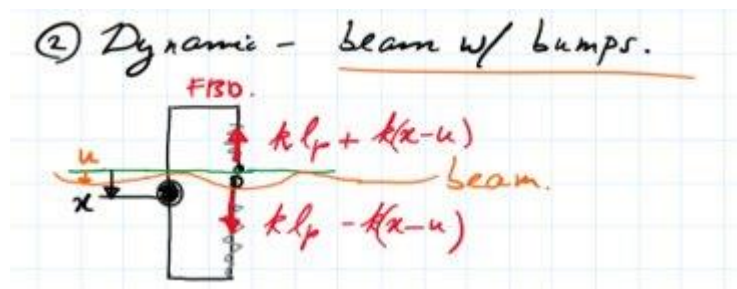


Figure 1818. FBD of a half model of horizontal stability

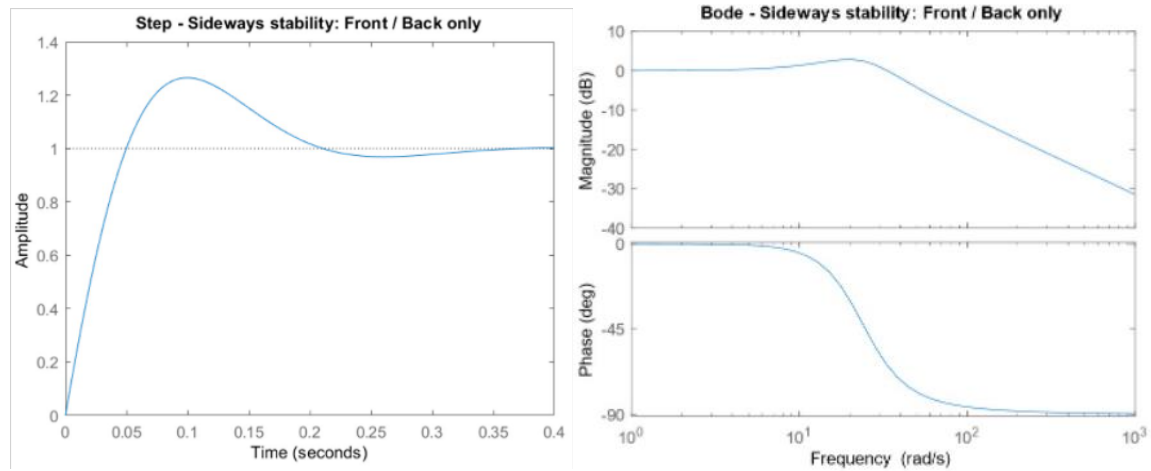


Figure 1919. Step response (left) and bode plot (right) of horizontal stability half model

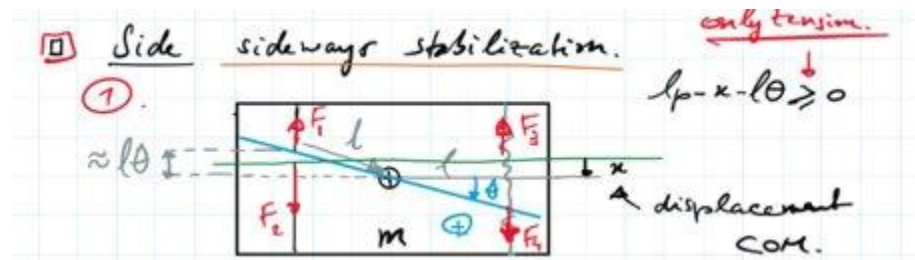


Figure 2020. FBD of full model of horizontal stability

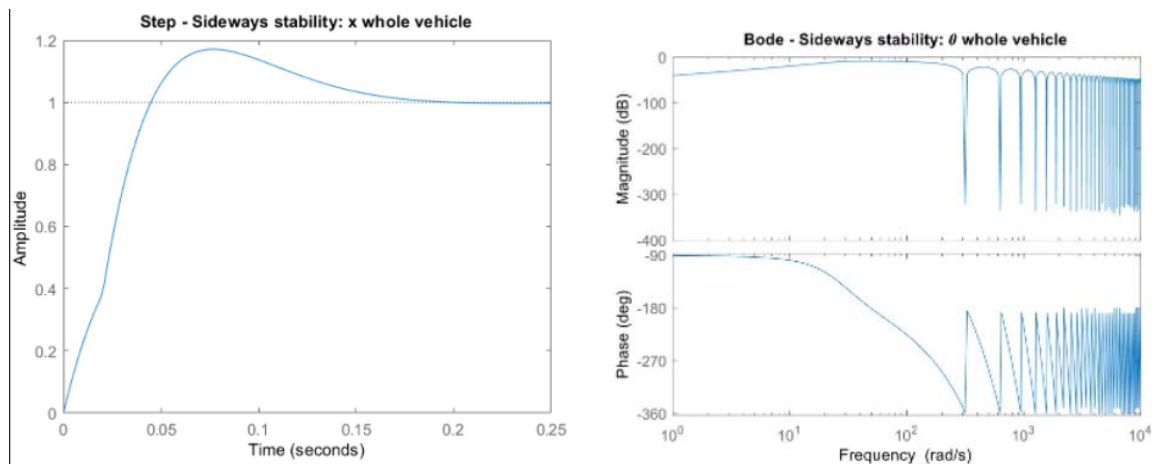


Figure 2121. Step response (left) and bode plot (right) of horizontal stability Full model

Powertrain

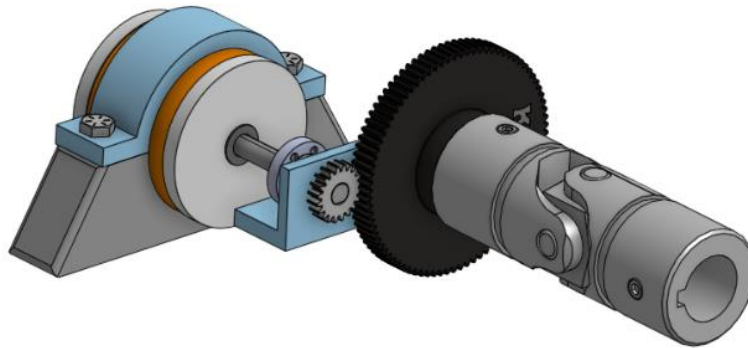


Figure 2222. Turnigy motor, gear train and universal joint transmission.

Choosing the right motor depended on a lot of factors such as power output and maximum acceleration of the pod. First, the types of motors were researched and the best type was chosen for our set up. Rather than a brushed DC motor, a BLDC motor was chosen to maximize efficiency and hence maximize power output. A BLDC motor with a KV constant of 125 RPM was chosen in order to maximize the torque per amp ratio. This would lead to a reduction in the required current and ohmic losses throughout the powertrain. Given these specifications and the consideration of cost, the Turnigy D5035-125KV Sensored Brushless Motor was chosen as depicted in Table 3.

Table 3: Motor Choices				
kV	MFR Part Number	Unit Cost	Total cost	Weight per motor (g)
125	D5035	\$ 120.0	\$ 480.00	745
37	HT-04	417	\$ 1,668.00	714
150	D6374	\$ 149.00	\$ 596.00	890

Using this motor, we calculated many other unknown constants of the propulsion system as shown in Table 4. Preliminarily, we set our acceleration as $0.5g$'s to reach our maximum pod velocity of 20m/s. Using the target speed and wheel diameter, the wheel RPM was determined to be 1273 RPM as seen in Equation 3 in the appendix. Using the wheel RPM, the motor RPM was calculated to be 5411 RPM as observed in Equation 4. Finally, the battery voltage was also calculated as 54 volts using the motor RPM and kV rating as seen in Equation 5 in the Appendix.

Table 4: Motor Calculations	
Specification	Value
Target Speed	20 m/s
Target Acceleration	$0.5 g$'s

Wheel Diameter	300 mm
Gear Ratio	4.25
Wheel RPM	1273 RPM
Torque per Wheel	36.75 Nm
Motor RPM	5411 RPM
Torque Per Motor	4.32 RPM
DC Link Voltage	54 V
DC Current per Motor	45.3 A

Assuming that the mass of the pod is around 100kg, we could also calculate the torque of the wheels in Equation X. The force part of the torque formula was calculated using target acceleration and mass of the pod while the radius used was the vertical stability wheel radius. This value was divided by 2 which was the number of wheels that were driven for vertical stability. The torque acquired for each wheel was 36.75Nm. The wheel torque also aided in calculating the motor torque since there were two motors for each wheel as listed in Table 4 above. The motor and wheel also had a gear ratio of 4.25 between them which was used in the calculation. Each motor was found to have a torque of 4.32Nm. Finally, using the motor and torque constants, the current per motor was calculated to be 45.3 amps by equating electrical power to mechanical power and solving for current draw.

Pressurized Systems

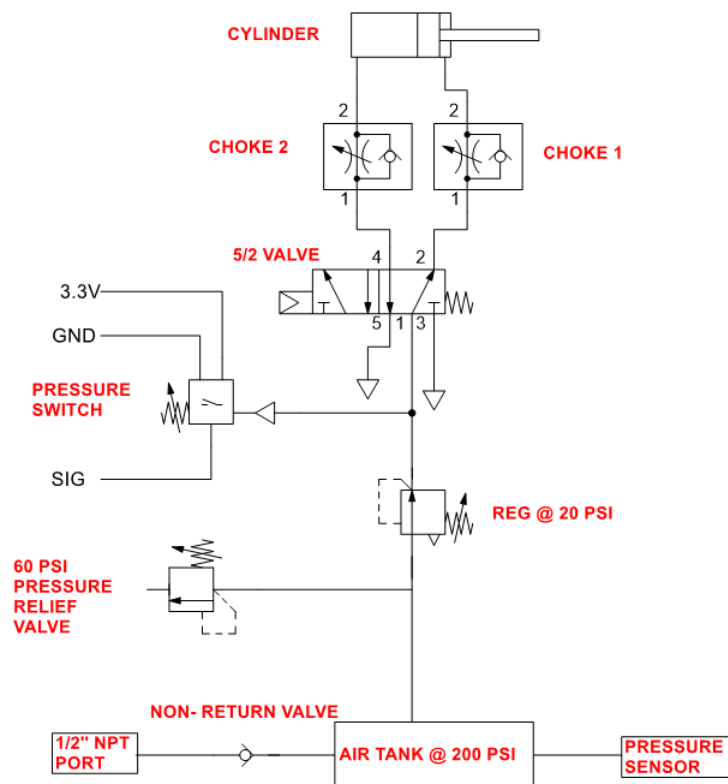


Figure 23. Pneumatic circuit diagram for the ECB

Pneumatic Actuation:

The actuation mechanism selected for the ECB is pneumatic actuation. Contrary to hydraulic and electric actuation, pneumatic was much more favorable in weight, efficiency, and safety.

Pneumatics can utilize mechanical solenoids and valves to transfer energy, while electric systems require electrical components powered by an active power source. Hydraulics would require heavy-duty cylinders, a pump, and large tanks to maintain high pressures due to the fluid being incompressible liquid. Contrary to the other two systems, pneumatics contain components that weigh less, conditioning the system to be more favorable under that category.

With regards to efficiency, the advantages of pneumatics outweigh the limitations. While electric actuators deliver a fast actuation speed and hydraulic exerts greater force against higher loads, pneumatic system proves to be more than sufficient for the ECB when tested with the automated test rig in both speed and force (minimum of 14 psi needed to actuate the ECB array).

Pneumatic systems are also safer. Both hydraulic and electric actuation requires an active power source, therefore in the event of a power loss, it would be impossible to actuate the brakes. Pneumatic actuation requires a passive power source, where air is stored in a tank. This would allow for actuations to take place amid power loss, rendering the system to be safe in the case of failure.

Pneumatic Circuit:

To limit excessive load on the overall pod, a compressed air canister is used to supply the pneumatic circuit with compressed air. The canister selected has 48 cubic inches volume and 3,000 psi max capacity (Tippman Paintball Tank). Despite the given parameters, the pneumatic circuit only needs 200-psi pressure in the tank, and a 50-psi outflow. This parameter is justified through testing with the brake dynamometer, which yielded a minimum pressure requirement of 14 psi to actuate the cylinder. A regulator is used to maintain a nominal output pressure at 20 psi, and a pressure relief valve to ensure that pressure does not exceed the 50-psi limit. To simplify the circuit, a non-return valve is used in exchange for a ball valve, therefore the valve discontinues air flow once it travels against the one-way flow.

Description of Actuation Method on ECB Brakes:

The pneumatic system integrated with brake assembly includes a single pneumatic linear actuator (Tie Rod air cylinder) that bridges between the two channels of magnet arrays. When the actuator is activated, the brakes are kept extended off the track (I-Beam). When the actuator is deactivated, springs attached to the structures connecting the two magnet arrays are released. In this state, the magnets are compressed over the track enabling an eddy current braking force to act on the I-Beam. The springs' natural tendency is to oscillate harmonically when released. Shock absorbers attached to the system act to dampen the oscillation of the springs at the very end of this first compression. This allows for the springs to function without initial resistance, and to make sure the brakes remain activated over the track.

Table 6: List of Pneumatic Parts			
Part Name	MFR Part Number	Description	Rated Pressure
5/2 Solenoid Valve 1/8 NPT	AVS-5211-24D	5 port 2-way valve to actuate brake cylinder	215 PSI
¼ NPT Hose	1593N1	Brass threaded rubber hose for connections	200 PSI
¼ NPT Brass Threaded Check Valve	7768K12	One way valve; turns off flow, once air flows backwards	500 PSI
¼ NPT Fast-Acting Pressure Relief Valve	4772K4	Turns off airflow at maximum pressure of 60 PSI	300 PSI
1/8 NPT Flow Control Valve	1FCRN	(Chokes) provides resistance to the airflow	175 PSI
1/8 NPT Pressure Switch	10M5307	Operating Range from 14-24 psi.	150 PSI
¼ NPT Regulator	AFR-2233-M	Air filter-regulator operating at 20 PSI	130 PSI
1/8 NPT Digital Pressure Sensor	QPSH-AP-42	Digital Air Pressure sensor	145 PSIG
48(ci) TIPPAMAN Paintball Tank	40319	Compressed Air Canister	3000 PSI

Braking

Eddy Current Braking Overview

The Eddy Current Brakes (ECB) were designed using arrays of permanent magnets and soft iron materials to help channel flux. Two different configurations of magnets are shown in Figure 23. In the first, upper and lower pairs of magnets are magnetized in the same direction and many flux lines follow a large loop with 4 magnets. In the second, upper-lower pairs are magnetized in opposite directions and most of the flux follows small loops with 2 magnets. FEMM simulations showed that the first (“aligned”) polarization produces more flux than the second (“opposed”), where more field lines intersect normally, generating a higher braking force.

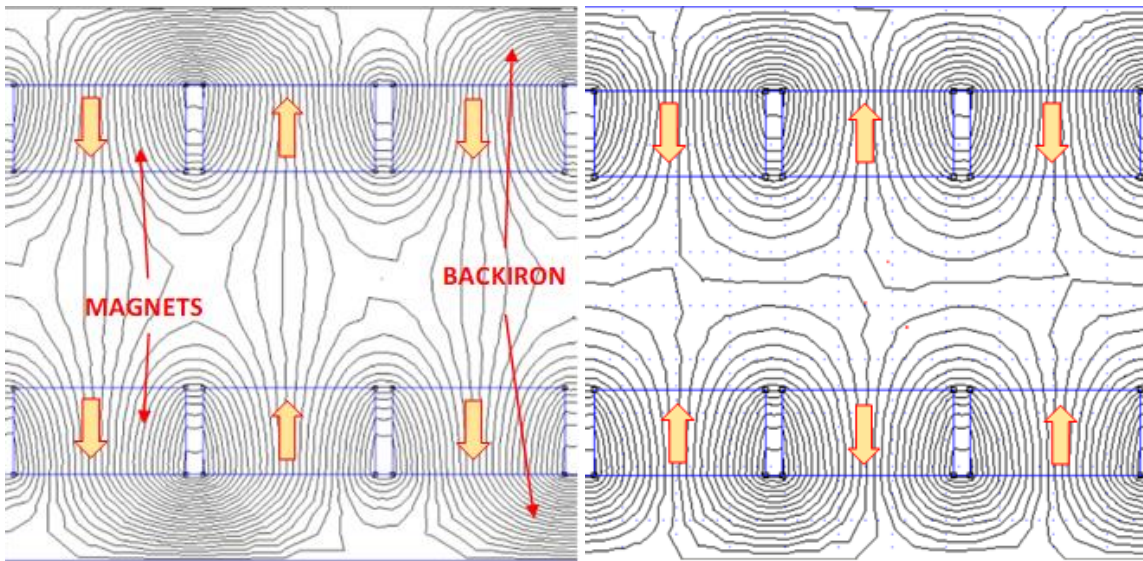


Figure 24. Magnetic fields of two separate arrangements of permanent magnets. The diagram on the left shows the field of upper and lower pairs with same polarity. The diagram on the right shows the field of the pairs with opposing polarity.

Since the backiron has a high relative permeability, the air/aluminum gap accounts for most of the reluctance in the magnetic circuit. Therefore, the width of the air gap should be minimized to increase the flux through the circuit. The lower limit on the air gap width is determined by the manufacturing tolerance of the test rig and, in the final pod design, the vertical stability tolerance. The aluminum bracket which supports the structure is designed with slots and through holes, so that the air gap width is adjustable during testing.

Typical backiron materials, such as laminated electrical steel, are dense. Therefore, to minimize the weight of the brakes in a full-scale pod, a material should be chosen with a high saturation point (so that a thin slice can be used instead of a thick slab) and a low density. The densities and saturation points of five materials are plotted in Figure 26. Saturation point is defined here as the point where μ is one hundredth of its original value. 1018 Steel was chosen because it has the highest saturation point to density ratio. It is also relatively inexpensive and easy to machine.

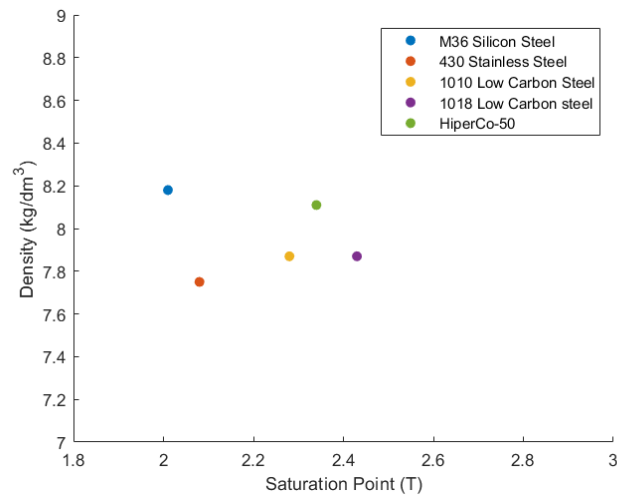


Figure 25. Saturation point vs density for magnetic materials

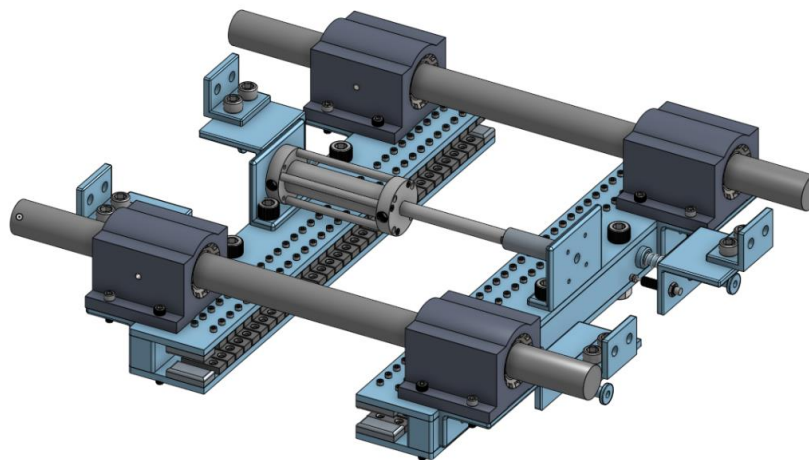


Figure 26. Full Eddy current braking system

Brakes Actuation

An asymmetrical activation of the brakes can create a moment on one side of the I-Beam, causing the pod to be imbalanced along the track. To prevent this issue, the brakes are activated concurrently and centered by their connection to the rest of the pod.

The springs used to connect the magnets to the pod are congruently arranged and of an identical model ($L = 3\text{in}$, $k = 5.1\text{ lbs/in}$) which additionally contributes to keeping the brakes centered during compression.

A single linear actuator system was primarily chosen for this reason. Having only one actuator allows for more control of timing, as the entire system does not need to be synchronous. With two or more pneumatic actuators, there are many more symmetries needed for the pistons to activate simultaneously, causing much more room for error.

With a single linear actuator, the brakes will extend equally as the piston produces an equivalent force on both ends. Notably, for the force to act evenly, the mass on both sides was set equal by adding weights to the end without the cylinder.

Safety Features

If the pod or the brakes system suddenly loses power, the linear actuator will be released, the brakes will mechanically be activated by the springs, and the pod will come to an emergency stop. A single linear actuator is preferable for this type of failure because if power is lost the brakes would activate on both sides, rather than potentially only one.

In future designs, friction brakes would be used along with the eddy brakes and would activate in case of system failure. Friction brakes would be also used to bring the pod to a complete stop as the eddy brakes lose effectiveness at slow speeds.

Battery System

Battery Selection

The first steps of the battery selection process included choosing between a lithium polymer (Li-Po) battery versus a lithium-ion (Li-ion) battery. Each had its own attributes, but the benefits of the lithium polymer version outweighed the benefits of the alternative. Li-Po batteries have four times the energy density of nickel-cadmium which makes them very lightweight and pliable. They also have a much higher discharge or 'C' rating, which is ideal for short runtimes. A low internal resistance, higher voltage, and a long-life cycle also made them the preferred choice.

The requirements for the system are shown in Table 7. Our battery selection process was driven by the need for a high discharge current. Having a high C rating allowed our pod to sustain a higher voltage at a higher current output, which meant that the pod would be able to accelerate rapidly. Another factor that was investigated was the total weight of the module since the pod would best benefit from a lightweight module that would not take up too much space. Considering all these attributes and narrowing down our choices between the models shown in table 8, we found the Tattu R-Line V3.9 to be a promising line of action. Connecting 4 of these cells in series would help acquire the necessary voltage, and the battery management system specifically developed for this module would monitor each cell's temperature and charge capacity.

Table 7: Power Requirements		
Voltage Range (V)	Max Current Draw (A)	Capacity
50-60	160	0.5

Table 8: Battery Selection Decision Matrix							
Model	Type	S/P	Total Voltage (V)	Total Current (Amps)	C Rating	Total Weight (kg)	Cost (\$)
Energus Li1x4p25RT	Li-ion	12S1P	57.6	180	18	3.584	912.00
Tattu Plus UAV	Li-Po	3S1P	66.6	240	15	6.189	660.00
Tattu R-Line V3.9	Li-Po	4S1P	60	186	120	1.354	133.74

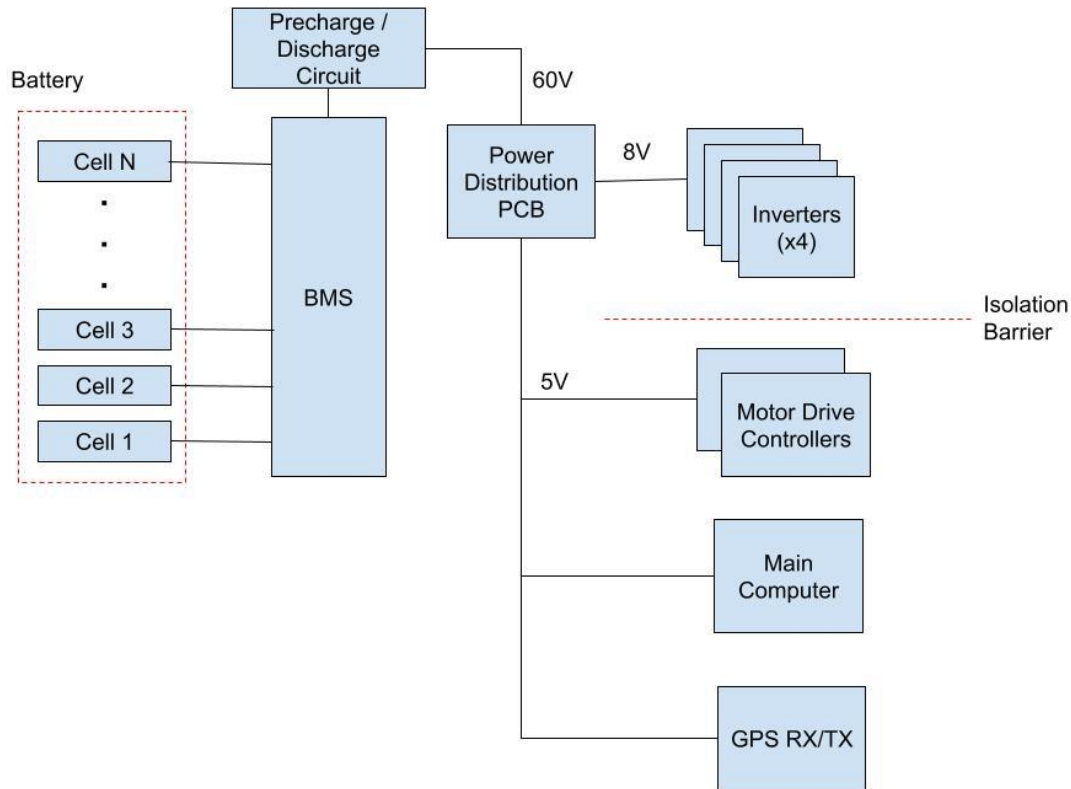
Battery Management System

A custom Battery Management System (BMS) will be designed to monitor cell voltages, balance cells during charging, and monitor cell temperatures during discharge. This PCB will be designed around the Renesas ISL94212 integrated circuit. This chip can monitor up to 12 cells in series, so two of them will be daisy-chained to accommodate the 16s battery pack. The PCB will connect to each of the four battery packs through their JST "charge" connectors, and will interface with the main onboard computer.

Electrical Systems and Wiring

High Level Description

In the high-power system, a maximum of 38 Volts AC (RMS) will be supplied to the 4 motors through 4 inverters. The low power system consisted of motor drive controllers, the main computer, and a GPS antenna. The appropriate voltages will be distributed throughout the system using a power distribution PCB.



Power Distribution PCB

A power distribution PCB, as shown in the figure below, was designed to power the inverters and provide isolated 5V rails for the onboard computer. The two “isolated” grounds are tied through a 1 MegaOhm ground tie resistor to prevent large voltage differences from occurring. XT60 connectors are used to interface with the battery pack and inverters. JST connectors are used to for low voltage connections. A CUI PQME3-D48-S5-M isolated regulator was used to step down the 60V to 5V for the logic supply.

Two power distribution PCB’s will be used – one to power the two motor drives attached to the front wheel, and one for the back wheel. This ensures that ohmic losses due to long wire harnesses are minimized.

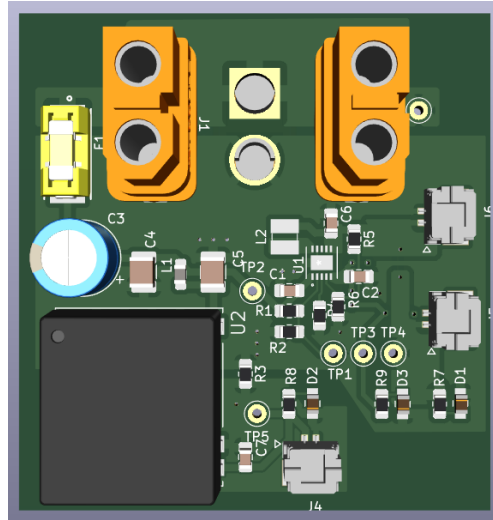


Figure 27: Power Distribution PCB

Motor Drive PCB

A custom-designed motor drive PCB, shown in the figure below, will be used to invert the DC link voltage and conduct closed-loop control of the four motors. Four of these PCB's will be required since each PCB controls a single motor. This modular approach was taken because it is easier to test and cheaper to replace broken parts. Two motor drives will be housed in a single enclosure along with a power distribution PCB. The enclosure will be 3D printed out of Formlabs' ESD Resin, which will protect against ESD and EMI.

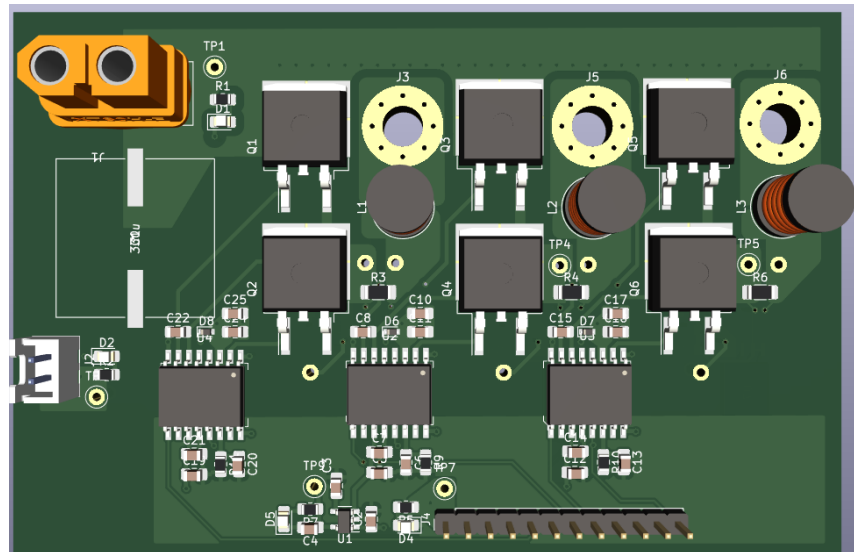


Figure 28: In-House Motor Drive

The schematic of the main part of the motor drive is shown below.

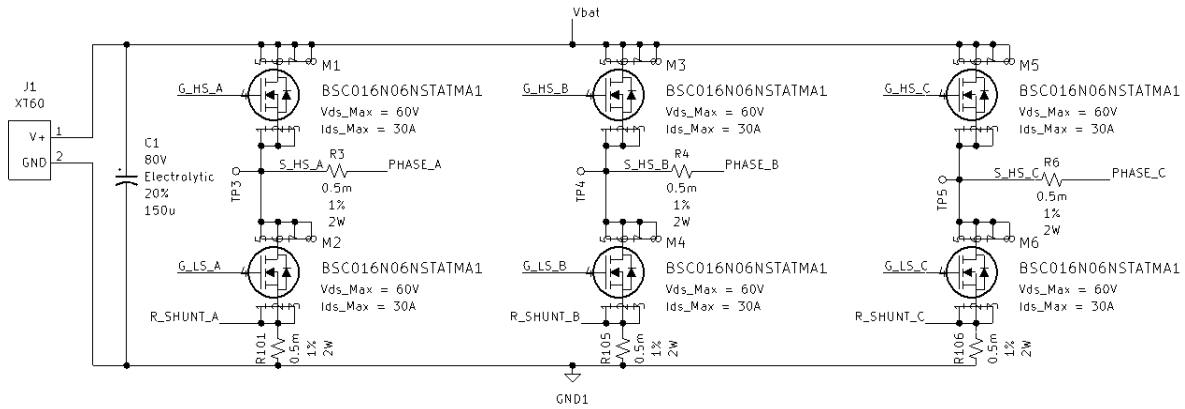


Figure 29: Inverter Circuit

The MOSFET's used as power switches have a maximum V_{ds} rating of 60V, which necessitates a voltage ripple of less than 5V on the DC link since the nominal battery voltage is 55V. To achieve this low voltage ripple, a large electrolytic capacitor is used on the DC link.

Shunt resistors are used for both current sensing (on each phase) and overcurrent detection (on the low side of each half bridge). The sensed current will be used for current-mode control by an external ESP-32 microcontroller, which will pass in the PWM signals to the gate drivers.

The gate drivers used are the Silicon Labs Si8234. These are isolated and can supply up to 4A instantaneous, resulting in minimal switching losses.

Safety Features

To protect the circuit from high inrush current, a precharge circuit will be utilized. This will consist of a high voltage contactor in series with a large resistor. will be switched on initially to charge the bypass capacitors in the motor drive.

In addition to this, overcurrent protection will be implemented in multiple ways. First, a 200A fuse will be connected in series with the battery pack to protect against any short circuit condition downstream of the battery pack. Second, a 55A fuse will be placed on the motor drive PCB. Third, the voltage across the low side shunt is compared to a threshold voltage, as shown in the circuit below. If the low-side voltage surpasses the threshold, the output of the comparator will drop low, disabling the gate drivers. Additionally, the comparators are latched within 10 ns of the fault occurring.

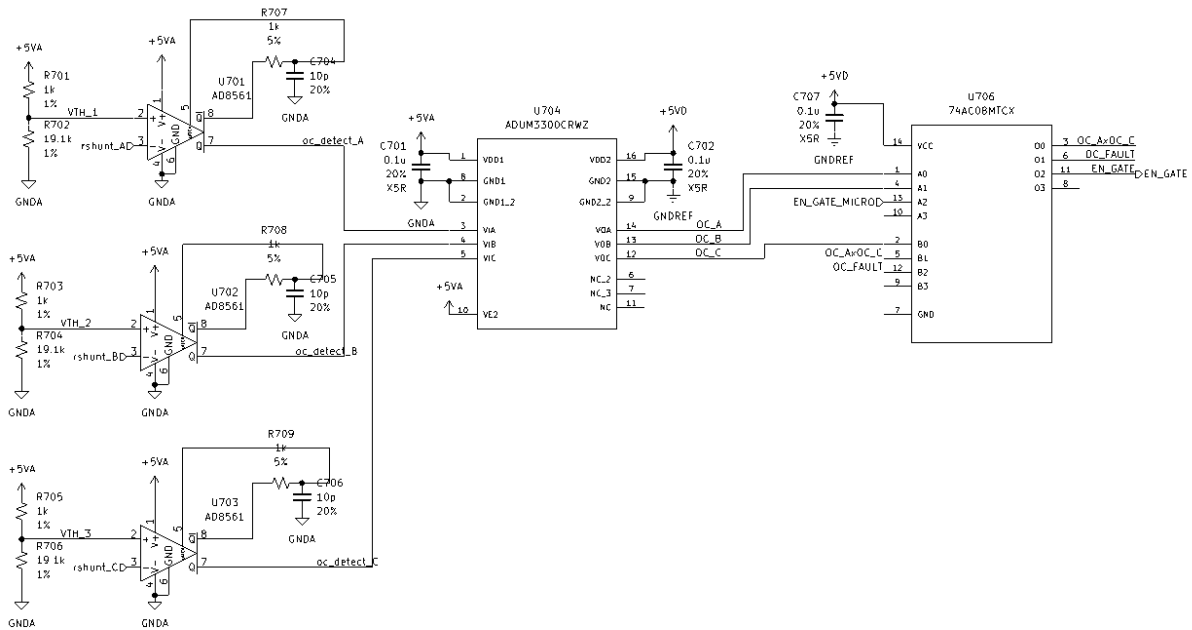


Figure 30: Overcurrent Protection Circuit

To design a simple form of an over-voltage protection circuit, a Zener diode having a maximum voltage rated slightly above the system's was placed at the output of the power supply. If the voltage exceeds its avalanche voltage, the diode will shut down the power line.

Software comms and controls

High Level Overview (Full Pod)

ESP32 microcontrollers are used to control the various parts of the pod. They are connected with each other and to a main onboard control computer with TCP/IP stack through on-board Ethernet connections or WiFi connections for low importance pure sensing microcontrollers. These microcontrollers will be used to control the various parts of the pod with safety critical systems, such as the brakes and motors getting two redundant microcontrollers that must work in synchrony, in order for the brakes to be disengaged or the motors to be respectively enabled.

The pod will have on board GPS receiver to track its location and speed as well as an Inertial Measurement Unit to keep track of the acceleration forces felt by the pod. Data received from all sensors including position, speed from a hall effect sensor, and acceleration from the IMU will be recorded onto an on board EEPROM.

The data will also be reported to the operator at a lower rate so they are aware of what the pod is doing.

On-Board Pod Control Computer

The on-board pod control computer handles controlling each aspect of the operation of the pod as well as the collection and analysis of data from various parts of the pod to ensure that they are within parameters. The OBPCC does all pre-drive checks and higher-level failure checks that rely on detecting discrepancies in complex data. Simpler failure checks are handled at the hardware level by the ESTOP board.

The operator will simply send a command to the OBPCC what they would like the pod to do, for instance, accelerate to a specific speed, then the OBPCC will do the state changes and actions required to fulfill that request.

Below is the state diagram describing the states that the OBPCC can be in. Note that the pod can always return to a safe state quickly on failure conditions.

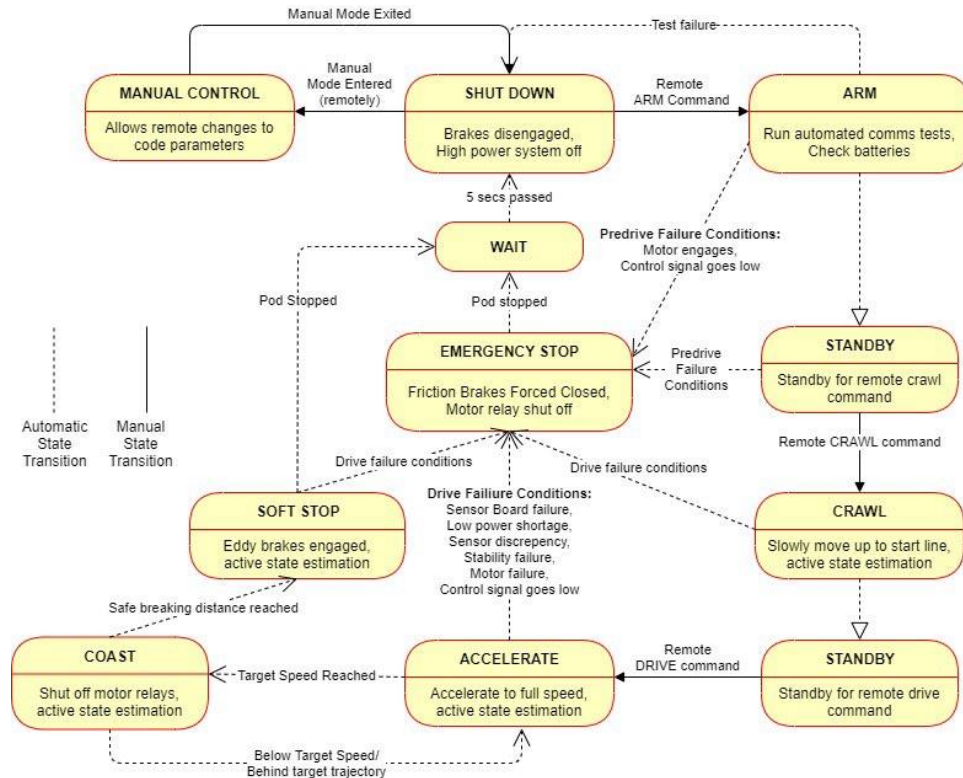


Figure 31. Full Pod State Diagram

There will also be a separate password protected debug mode which will provide the operator direct access to the microcontrollers that the OBPCC commands. This can be disabled for cases in which the pod will be running in a possibly untrusted environment.

Communication Between OBPCC and Controlling Computer

Communication between the controlling computer and the primary on board pod control computer will be done via Protobuf messages over a TCP connection. Many different communication protocols were considered for communication for the brake dynamometer test rig and we settled on the ESPHome native API which works with Protobuf messages. While we will not use the ESPHome native API for communication with the controlling computer on the full pod, we found Protobuf messages over TCP to be a very reliable and low latency way to transfer messages without risk of errors and we already made the logic required for handling disconnection on the brake dynamometer test rig which we can reuse for the full pod.

The wireless communication between the OBPCC and controlling computer is an issue that we are currently considering. Some options that we are considering include WiFi with signal amplifiers, communication on some unregulated radio band, or communication in an amateur radio band as several of our members are licensed amateur radio operators.

Contingencies

The microcontrollers are programmed to expect a safety ping from the primary on board pod control computer at a configurable rate. If this interval is missed, the microcontroller will assume that it has lost

communication with the OBPCC because it has either crashed, disconnected, or is otherwise unavailable and will transition into the safest possible state for that microcontroller. To return to normal operation, the operator will need to reconnect and reset the safe mode.

The ESTOP board is also critical to ensure that having only some microcontrollers lose connection and drop into safe mode does not cause an issue. If, for instance, the brake microcontroller goes into safe mode and engages the brake, the ESTOP board will also open the relay for the motor.

For especially critical systems like the motor and brake controls, redundant microcontrollers are used that a watchdog board monitors to ensure that only commands that are agreed upon by both microcontrollers are passed to the actual system. If there is a disagreement, the watchdog board will cease its all-clear signal which will cause the E-Stop board to begin an emergency stop.

We are also considering the possibility of having a secondary on-board pod control computer for redundancy, running the same software. A separate system will monitor the outputs of both pod control computers and ensure that they are identical. If the PCCs disagree, an emergency stop will be initiated. This will ensure that random occurrences such as bit flips cannot result in an accident.

Appendix

Frame FEA responses

(I) Downward force applied on hollow square beam

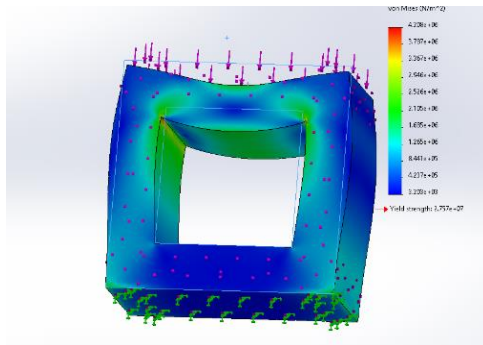


Figure 1: Von misses stress analysis results

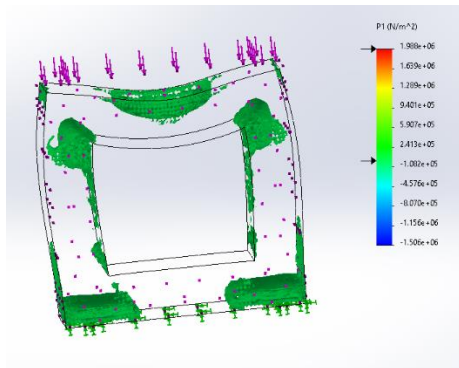


Figure 2: Graphic of critical areas of interest using nodal highlighting.

(II) Downward force applied on a C bracket

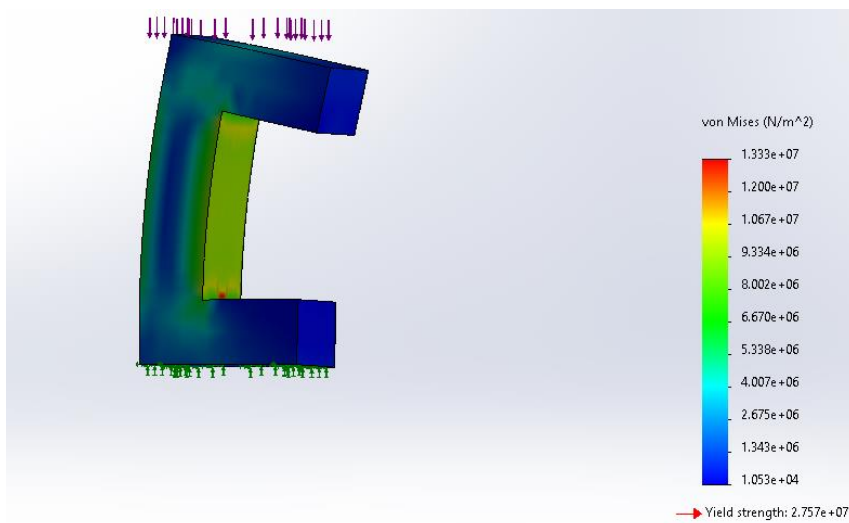


Figure 3: Von misses stress analysis results

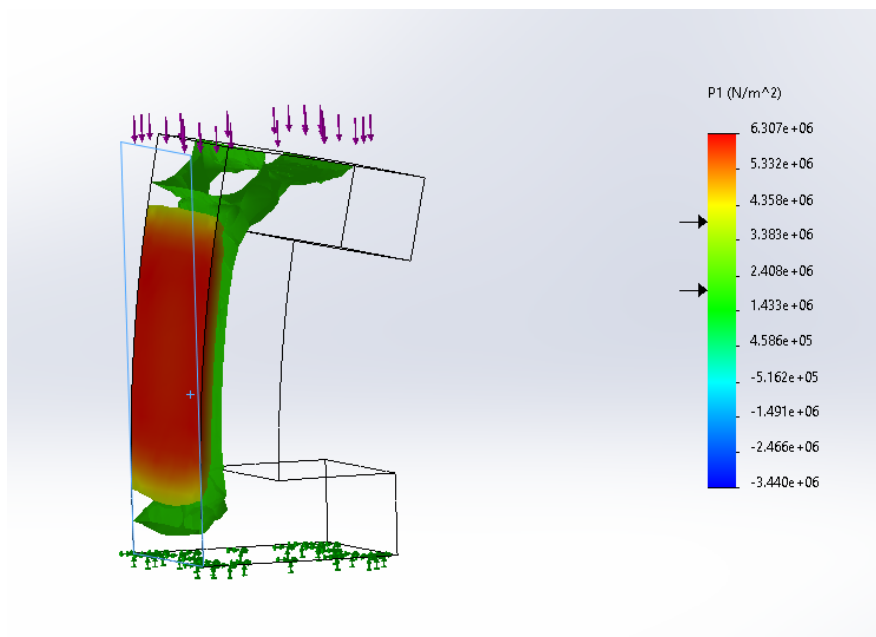


Figure 4: Graphic of critical areas of interest using nodal highlighting.

(III) Axial force applied on hollow square beam

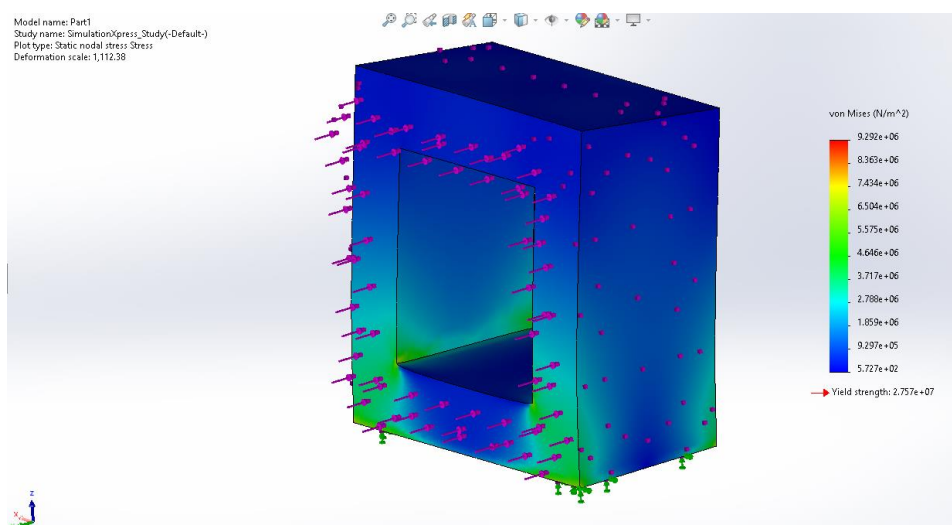


Figure 5: Load applied axially, no failure indicated

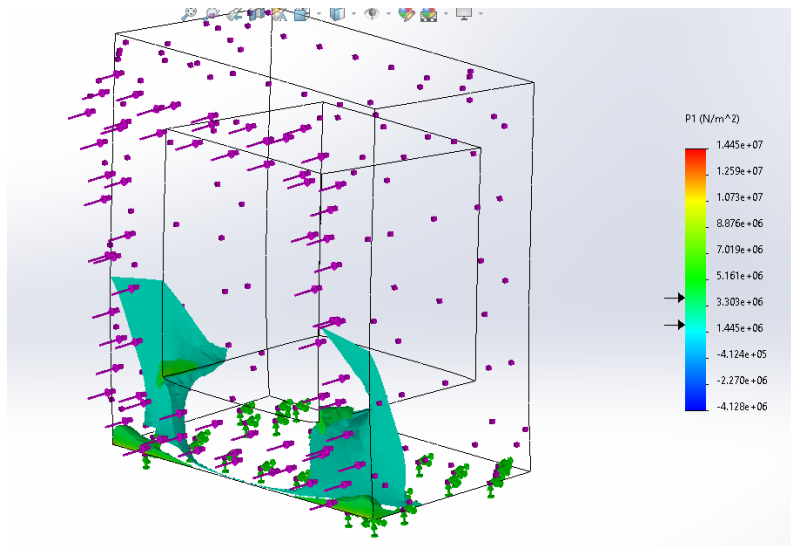


Figure 6: Graphic of critical areas of interest using nodal highlighting.

(IV) Axial force applied on C bracket

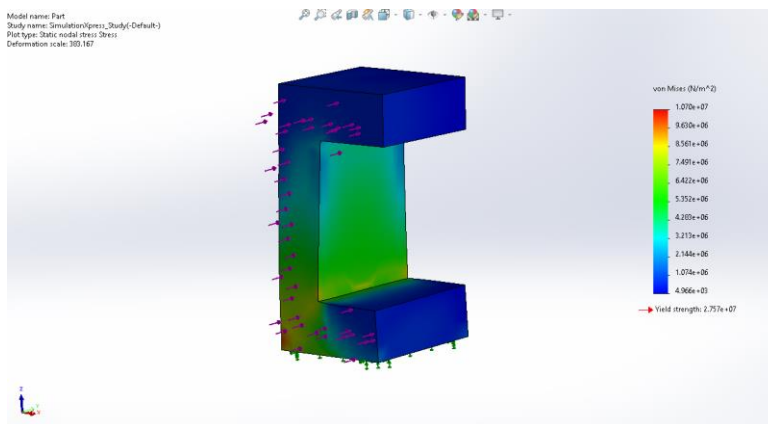


Figure 7: Load applied axially, no failure indicated

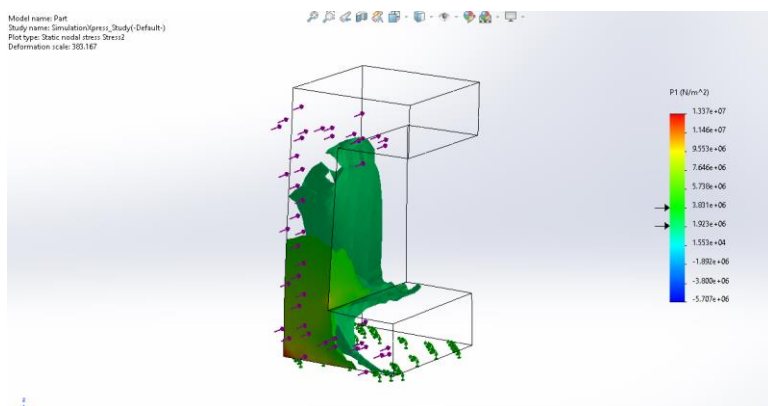


Figure 8: Graphic of critical areas of interest using nodal highlighting.

Stability Mechanical Analysis

Equation 1: Friction coefficient between wheel and track

$$\begin{aligned}
 W &= \frac{1}{2}mv^2 \\
 \frac{1}{2}mv^2 &= F_f d \\
 \frac{mv^2}{2d} &= \mu mg \\
 \frac{v^2}{2dg} &= \mu \\
 \frac{(20 \text{ m/s})^2}{2(100\text{m})(9.81 \text{ m/s}^2)} &= \mu \\
 \mu &= 0.2040
 \end{aligned}$$

Equation 2: Radius of driven wheel derivation

$$\begin{aligned}
 \tau &= I * \alpha \\
 \tau &= \left(\frac{1}{2}MR^2\right)\left(\frac{a}{R}\right) \\
 \tau &= \left(\frac{1}{2}MRa\right) \\
 R &= 11.77 \text{ inches}
 \end{aligned}$$

Equation 3: Wheel RPM calculation

$$\begin{aligned}
 \omega_{wheel} &= \frac{60 \times v_{target}}{\phi_{wheel}/(1000\pi)} \\
 WheelRpm &= \frac{60 \times TargetSpeed}{WheelDiam/(1000\pi)} \\
 WheelRpm &= \frac{60 \times 20\text{m/s}}{300\text{mm}/(1000\pi)} \\
 WheelRpm &= 1273\text{rpm}
 \end{aligned}$$

Equation 4: Motor RPM calculation

$$\omega_{motor} = GR * \omega_{wheel}$$

$$MotorRPM = GearRatio \times Wheel\ RPM$$

$$MotorRPM = 4.25 \times 1273rpm$$

$$MotorRPM = 5411rpm$$

Equation 5: Battery voltage calculation

$$V = \frac{\omega_{motor}}{KV_{factor} \times \tau_{factor}}$$

$$Battery\ Voltage = \frac{MotorRPM}{KVRating \times TorqueRatingFactor}$$

$$Battery\ Voltage = \frac{5411rpm}{125kV \times 0.8}$$

$$Battery\ Voltage = 54volts$$